Using time-resolved penumbral imaging to measure low x-ray emission signals from capsule implosions at the NIF

Bishel, D. T.; Bachmann, B.; Yi, A.; Kraus, D.; Divol, L.; Falcone, R. W.; Fletcher, L. B.; Glenzer, S. H.; Landen, O. L.; Macdonald, M. J.; Masters, N.; Neumayer, P.; Redmer, R.; Saunders, A. M.; Witte, B.; Döoppner, T.;

Originally published:

October 2018

Review of Scientific Instruments 89(2018)10, 10G111

DOI: https://doi.org/10.1063/1.5037073

Using time-resolved penumbral imaging to measure low x-ray emission signals from capsule implosions at the NIF[a)]

D.T. Bishel,[1] B. Bachmann,[1] A. Yi,[2] D. Kraus,[3] L. Divol,[1] R.W. Falcone,[4,5] L.B. Fletcher,[6] S.H. Glenzer,[6] O.L. Landen,[1] M.J. MacDonald,[4] N. Masters,[1] P. Neumayer,[7] R. Redmer,[8] A.M. Saunders,[4] B. Witte,[6,8] and T. Döppner[1]

[1)] *Lawrence Livermore National Laboratory, Livermore, USA*
[2)] *Los Alamos National Laboratory, Los Alamos, USA*
[3)] *Helmholtz-Zentrum Dresden-Rossendorf, Dresden, Germany*
[4)] *University of California, Berkeley, USA*
[5)] *Lawrence Berkeley National Laboratory, Berkeley, USA*
[6)] *SLAC National Accelerator Laboratory, Menlo Park, USA*
[7)] *Gesellschaft für Schwerionenphysik, Darmstadt, Germany*
[8)] *Universität Rostock, Rostock, Germany*

(Dated: 29 March 2018)

We have developed an experimental platform at the National Ignition Facility to measure x-ray Thomson scattering (XRTS) spectra from indirectly-driven capsule implosions that create extreme density conditions near stagnation [D. Kraus et al, J. Phys. Conf. Series **717**, 012067 (2016).]. In order to account for shot-to-shot variations of the stagnation time and to benchmark the achieved plasma conditions between shots and against radiation hydrodynamics simulations, we need to know the relative timing between the scattering measurement and the peak x-ray emission, which occurs at stagnation. Due to lower implosion velocity, use of a low gas fill capsule, and hot spot symmetry perturbations, the hot spot emission is $100 - 1000$x weaker than that of standard ICF implosions. To address this challenge, we have developed and fielded a new pinhole-imaging snout that exploits time-resolved penumbral imaging. Using 150 μm diameter penumbral-imaging pinholes, a time series of 2D images can be reconstructed through analysis of the penumbras. The reconstructions allow us to extract the spatially and temporally resolved evolution and timing of the implosion through stagnation. We use differential filtering to extract plasma temperatures, additionally constraining the thermophysical plasma conditions. Despite fluctuations of the x-ray flash intensity of up to 5x, the emission time history is similar from shot to shot, and slightly asymmetric with respect to peak x-ray emission. Peak emission times vary by up to 250 ps and can be determined with an accuracy of 50 ps.

I. INTRODUCTION

The regime of warm dense matter (WDM) broadly encompasses densities within two orders of magnitude of solid density and temperatures up to 10s of eV, present in astronomical objects such as brown dwarfs and planet interiors[1]. Due to the difficulty of achieving such conditions in the laboratory, WDM has only recently been studied in detail. X-ray Thomson scattering (XRTS) is a particularly useful tool for studying WDM, as both the electron temperature and electron density can be inferred from a single spectrum[2]. We have developed an experimental platform at the National Ignition Facility to measure XRTS spectra from extremely dense CH in indirectly-driven capsule implosions near stagnation[3,4]. The XRTS spectra are resolved using the Mono-Angle Crystal Spectrometer[5] and recorded by a framing camera. Given the sub-nanosecond duration of the stagnation event, the framing camera must be precisely triggered to capture spectra from the highest densities achieved during the experiment.

However, prediction of the stagnation time t_{st} is non-trivial; the capsule trajectory is sensitive both to design differences (e.g. capsule construction and requested laser drive) and stochastic fluctuations (e.g. capsule surface imperfections and delivered laser drive). These shot-to-shot variations influence the absolute time of stagnation and confound any direct comparison of measured densities between shots. Furthermore, the x-ray flash and the extreme density at stagnation preclude implementation of radiography to measure the core radius as a function of time to infer t_{st}. To account for shot-to-shot variations in capsule trajectory, we exploit the x-ray self-emission of the stagnating core as a timing fiducial, enabling a more informative comparison between experiments. Though x-ray detectors exist at the NIF for ICF purposes, the lower implosion velocity, lower gas fill, and hot spot symmetry perturbations in our high density experiments produce reduced hot spot temperatures, decreased volumes, and elevated densities compared to typical ICF implosions; consequently, x-ray emission is weaker by two to three orders of magnitude. The standard suite of x-ray detectors available at the NIF are insufficient for measuring these low x-ray signal levels. To compensate for the expected decrease in x-ray emission from the stagnated core, we have developed and fielded a new pinhole-imaging snout (Figure 2) that employs time-resolved penumbral imaging[6–8].

[a)] Contributed paper published as part of the Proceedings of the 22nd Topical Conference on High-Temperature Plasma Diagnostics, San Diego, California, April, 2018.

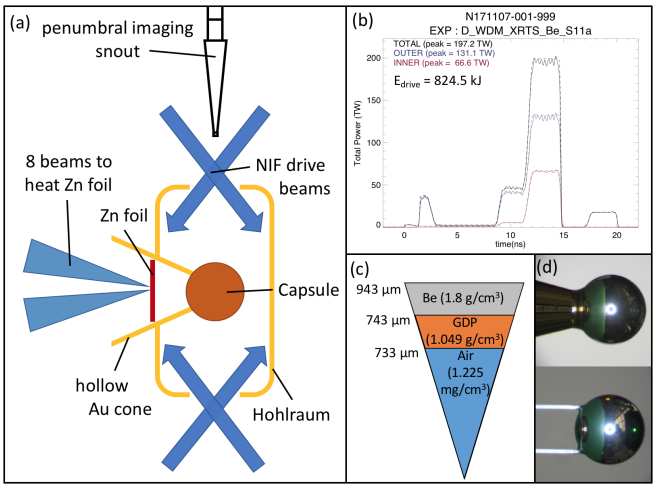

FIG. 1. (a) Experimental design, shown for a Au cone supported capsule. Not to scale. For details on the snout, see Figure 2. (b) Requested and delivered laser drive; for details, see text. (c) Schematic of nominal Be capsule. (d) Photographs of as-built capsules with Au cone (top) and HDC stalk (bottom) supports.

In Section II we introduce the experimental campaign for which the diagnostic was developed. In Section III we outline the pinholes, filters, and detector used in the new diagnostic. In Section IV we present the results of a recent experiment that fielded the diagnostic, demonstrate the use of x-ray self-emission as a time fiducial, and compare the experimentally derived plasma temperature and core size to hydrodynamic simulations. Conclusions and final statements are included in Section V.

II. EXPERIMENTAL CONSIDERATIONS

This diagnostic has been fielded on indirect-drive spherical capsule implosions at the NIF that sought to collect x-ray Thomson scattering (XRTS) signals from CH and Be at high density ($n_e \approx 10^{25} cm^{-3}$). Here, we focus on Be capsule implosions. The air-filled capsules had two layers, an inner 10 μm-thick plastic layer and an outer 100 μm-thick Be layer. The plastic layer was made from glow discharge polymer (GDP)[10]. For additional details, see Figure 1(c). The experiments used room-temperature gas-filled Au hohlraums with diagnostic windows along the MACS line of sight. The window between MACS and the target (90-68) is a standard viewing window, while the window across from MACS (90-248) eliminates the direct view of the hohlraum wall that the spectrometer would otherwise have. 184 NIF beams were used to drive x-ray production in the hohlraum; 8 beams were reserved for heating a Zn foil to produce He-α x-rays for Thomson scattering after the main laser drive. (DRIVE DESCRIPTION: $\Delta\lambda$, Figure 1(b)). This drive was derived from earlier Be tuning shots **??**.

The capsules were supported in the hohlraum by one of two separate schemes (Figure 1(d)). The cone support scheme holds the capsule at the hohlraum center via a hollow Au cone. The base of the cone is affixed to the inner face of the hohlraum wall, and the tip is glued to the capsule surface. In experiments that used the cone support, the cone housed the Zn foil x-ray source and contained blow-off plasma from the foil. This experimental target design was derived from the hydrogowth-radiography (HGR) platform, which explored cone-mounted capsules in detail[11,12]. However, use of the cone support when measuring XRTS at scattering angles less than 45° was projected to become a liability as the tip of the Au cone would have a direct line of sight to the XRTS spectrometer. The resulting scattering and emission from the heated Au cone would spoil the XRTS spectrum, thereby disqualifying the cone support from use at small angles.

The stalk support scheme uses two 0.085 mm square, 1.7 mm long high-density carbon (HDC) stalks anchored to the hohlraum wall to suspend the capsule within the hohlraum. The slender, low-Z stalks produce negligible x-ray emission in our spectral region of interest. Changing to the stalk support scheme mitigates the detrimental noise sources that emerge at small scattering angles, making the stalks more suitable for XRTS at small angles.

III. METHODS

A schematic of the snout assembly is shown in Figure 2. The nose cone of the snout is outfitted with a standard collimator that serves as a large-diameter pinhole array (Figure 2(b)), increasing throughput by a factor of 100 over the more common 10 μm pinholes[6,7]. Constructed from 500 μm thick Ta, the collimator mask stands 95 mm from target chamber center (TCC) to provide a 13x magnification. Each penumbral aperture is checked for circularity and is found to vary by less than X.X % of the average radius. The resulting penumbral images are analyzed and reconstructions are performed as described in ref. 7. The pinhole images are attenuated by multiple polyimide films and then projected onto the Gated X-ray Detector (GXD)[13,14], a 4-strip variable delay framing camera fiber-coupled to a CCD, which is mounted behind the snout assembly. Each strip is streaked in time over 240 ps with an integration time of 100 $\pm$ 5 ps[15]. As a result, each pinhole image is recorded at a different time during the implosion. Representative raw data is included in Figure 2(d).

The filtering package is much lower than standard configurations because it was optimized to increase signal by five- to ten-fold while still shielding the detector from debris ejected from the target chamber. The final stage of polyimide filters is separated into six 25 μm filters, as this is thought to provide better shielding than a single 150 μm filter. An optional 1 mm differentially filtering polyimide strip mask (Figure 2(c)) is also available. The

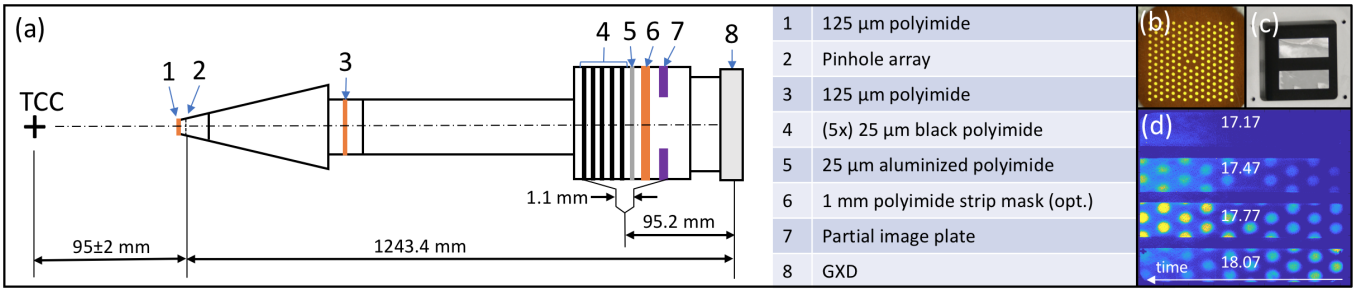

FIG. 2. (a) Schematic of penumbral imaging snout. Filtering elements are listed in the adjoined table. Note that the filtering stack (4 through 7) is assembled without any separation between its elements. The image plate (7) records time-integrated emission around the GXD for photometric calculations. (b) Photograph of the pinhole array (1 and 2). (c) View from the rear of the snout. The strip mask is visible in black. (d) Raw data from N170214 that was recorded without the strip mask. The time in nanoseconds corresponding to the central pixel of each strip is shown. The time at which each pixel is recorded increases from right to left. When the strip mask is included, half of the center two strips is filtered.

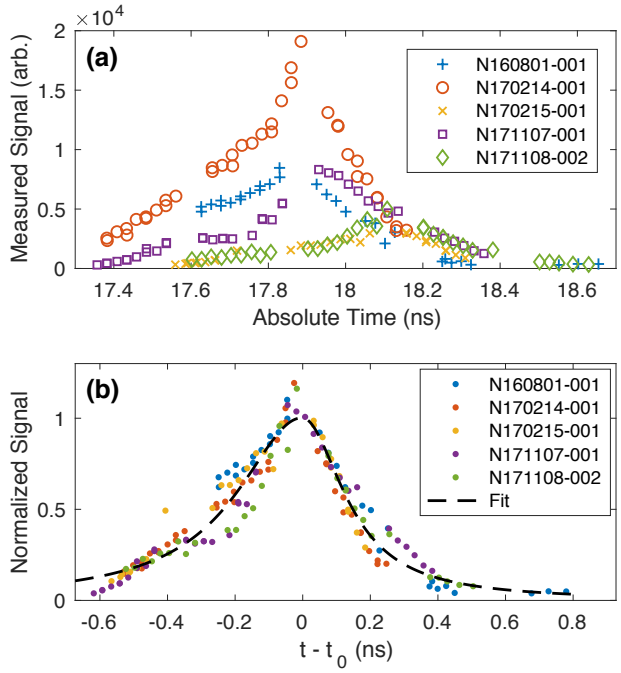

FIG. 3. (a) Background subtracted, flat-field corrected self-emission against absolute time from multiple shots. Each data point is taken from a different pinhole image. Peak emission time of each shot is inferred from the corresonding dataset. (b) Normalized self-emission against time from peak emission. The dashed line is a fit to the two-sided Lorentzian of Equation 1 for all of the data shown. Since the composite FWHM (380 ps) is significantly larger than the gate pulse width (100 ps), time blurring is negligible.

mask filters half of strips 2 and 3, and, when the mask is included, the ratio between the filtered and unfiltered signals allows inference of the radiation temperature of the core[9].

IV. RESULTS

From the penumbral images of the hot spot recorded by the GXD, we can track x-ray self emission in time and thus identify the time of peak x-ray emission for each shot (Figure 3(a)). We use "flat-field" measurements to correct for differences in gain along a given strip (voltage droop) and between strips. When plotting flat-field corrected self-emission versus time from peak emission and normalizing to the integrated area of this curve (Figure 3(b)), we find that self-emission time histories relative to peak emission are consistent between shots, regardless of the absolute time of peak emission. The absolute time of peak x-ray emission differed between shots by as much as 250 ps – roughly half the FWHM of the self-emission signatures – whereas the shape of the emission time histories remains similar, indicating equivalent implosion dynamics between shots (see Table I). These similarities between shots suggest that a more robust time history of self-emission can be constructed by aligning the individual time histories relative to their respective peak emission and normalizing the signal intensity. The resulting dataset can be approximated by a two-sided Lorentzian function $L(t-t_0)$, given by

$$L(t-t_0) = \begin{cases} \frac{(\Gamma_l/2)^2}{(t-t_0)^2+(\Gamma_l/2)^2} & t-t_0 \leq 0 \\ \frac{(\Gamma_r/2)^2}{(t-t_0)^2+(\Gamma_r/2)^2} & t-t_0 > 0 \end{cases} \quad (1)$$

with centroid t_0 and full-width at half-maxima (FWHM) of the left and right wings Γ_l and Γ_r, respectively. t_0 corresponds to the time of the x-ray flash. The function is normalized such that $L(0) = 1$.

The FWHM $\frac{\Gamma_l+\Gamma_r}{2}$ of the emission feature is found to be roughly 380 *ps* (see Table II). Although the measured signal is in reality a convolution of the x-ray emission and the gate pulse of the GXD, the time width of the gate pulse (100 *ps*) is sufficiently shorter than that of the emission to be considered negligible. As a reasonable approximation, we assume the measured signal is negligibly

different from the true x-ray emission profile.

Comparison with time-resolved hydrodynamic simulations (Figure 4) suggests that the measured time of peak self-emission corresponds to the time of peak density of the capsule core. Furthermore, peak density of the Be shell occurs within 0.5 ns after peak core density. This motivates probing the Be shell with x-rays shortly after peak self-emission in order to measure XRTS from the highest densities achieved.

Using the optional differential filtering mask, we calculated a radiation temperature of 500±50 eV, which is in reasonable agreement with hydrodynamic simulations (Figure 4). Multiple sources factor into the large uncertainty. First, there is a signal to noise issue, making the signal above background difficult to discern in the filtered region. Second, the hot spot images are recorded at discretized times, requiring that we choose the image nearest to peak emission as an estimate of temperature at peak emission. Finally, inference of an electron temperature depends strongly on the opacity of transmitting materials between the emitting core and the detector. Because opacity is known to decrease with increasing ionization, we expect that the opacity of the heated Be shell at stagnation is some fraction of the cold opacity, but the exact relation to temperature of the effect is unknown. If one assumes that the opacity of Be at stagnation drops to 50% of cold opacities, the inferred temperature rises by roughly 25%. Our inferred temperature then stands as a lower bound with respect to opacity effects. The corresponding sensitivity plots are shown in Figure 5.

Figure 6 shows the time history of the spatially resolved, reconstructed penumbral images. The penumbral analysis indicates a mostly round emitting region with a perturbation in the direction of the support stalks. We observe a possible symmetry axis extending from the bottom left to the top right of each image, roughly coinciding with the stalk and diagnostic window axes. Comparing to the hydrodynamic simulation in Figure 4, we see that the extent of the x-ray emitting region is within the $\approx 70\mu m$ inner radius of the compressed Be shell.

TABLE I. Values used to align self-emission data. For a decrease in the MCP bias voltage of 20 V, the gain is expected to increase by a factor of $3^{\frac{20V}{50V}} \approx 1.55$; this relative gain is accounted for in the displayed amplitudes.

Shot	t_0 (ns)	Δt (ns) to N160801	Amplitude (a.u.)	Bias (V)
N160801-001	17.88	0.00	2.5	200
N170214-001	17.91	0.04	4.6	200
N170215-001	18.13	0.25	1.0	200
N171107-001	17.98	0.10	3.7	220
N171108-002	18.13	0.25	1.9	220

TABLE II. Fit parameters of a 2-sided Lorentzian to the combined dataset. The amplitude A is included as an additional fit parameter to allow for errors in normalization.

Parameter	Fitted Value
$\Gamma_l(ns)$	0.47 ± 0.04
$\Gamma_r(ns)$	0.30 ± 0.03
$t_0(ns)$	0.0 ± 0.01
$A(ns)$	1.00 ± 0.03

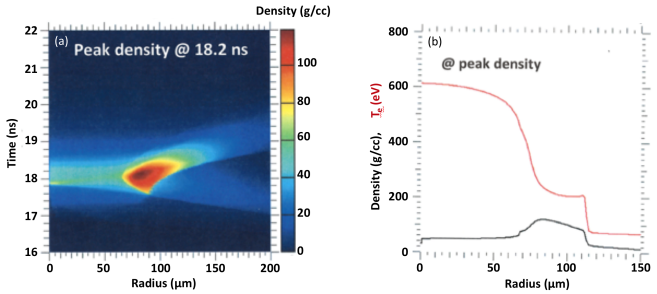

FIG. 4. Simulation of (a) density profile (color) as a function of time and (b) density and temperature profiles at peak density for the experimental conditions of N160801-001. The inner radius of the Be shell extends to roughly 70 μm at stagnation. The simulation assumes a laser duration of (coast time of 2.9 ns), while the experiment used a duration of (coast time of 3.1 ns). Peak core density occurs around 17.8 ns, compared to the peak self-emission measured as 17.875 ns.

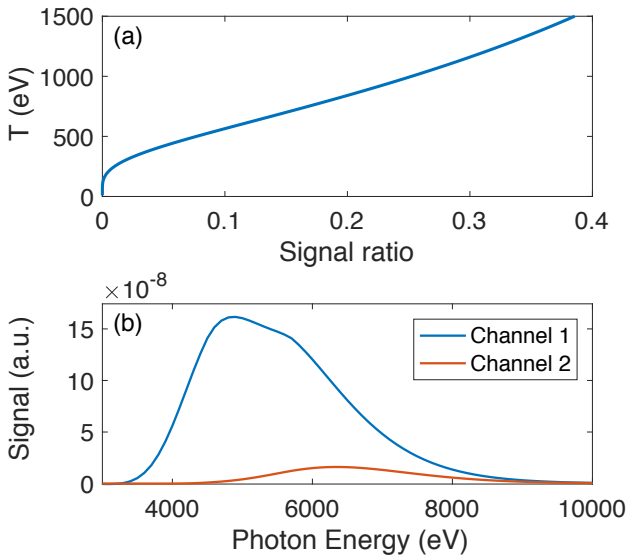

FIG. 5. (a) Inferred temperature as a function of the measured ratio between the filtered and unfiltered emission signals. We measure a signal ratio of 0.08, corresponding to a hotspot temperature of $T \approx 500$ eV. (b) Sensitivity curve of the spectrally-integrating detector, assuming the inferred temperature of 500 eV. The spectra are corrected for attenuation by the compressed capsule, attenuation by the installed filtering configuration, and the spectral response of the detector.

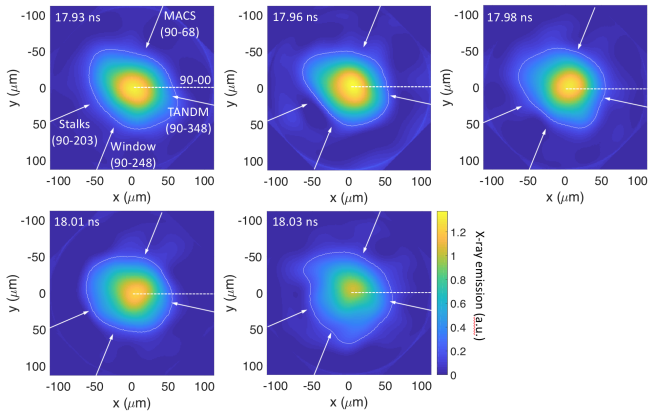

FIG. 6. A sequence of time-resolved x-ray images of the stagnated core of N171107-001 near peak emission, reconstructed from the measured penumbra. The reconstructions are plotted in the same colormap and are blurred to have a spatial resolution of 20 μm. The 17% contours are drawn in white, demarcating the x-ray emitting core. The directions of the support stalks and the windows (in front of and across from MACS) are shown because they constitute possible sources of symmetry perturbations. The target positioner (TANDM) is noted for completeness.

V. CONCLUSION

We have fielded a new low-intensity, x-ray penumbral imaging snout on a series of experiments. We report similar self-emission time histories relative to stagnation across multiple shots, providing a timing fiducial useful for comparing different shots despite shot-to-shot variations in stagnation time. Differential filtering suggests plasma temperatures of 500 eV at peak x-ray emission. The reconstructed x-ray images indicate a mostly round emitting region with a 50 μm radius. Comparing to hydrodynamic simulations, we observe that peak self-emission occurs simultaneously with peak core density and less than 0.5 ns prior to peak shell density. [Statement on next applications of this instrument? measurements that are now possible?]

ACKNOWLEDGMENTS

This work performed under the auspices of the U.S. Department of Energy by Lawrence Livermore National Laboratory under Contract DE-AC52-07NA27344 and supported by Laboratory Directed Research and Development (LDRD) Grant No. 18-ERD-033.

[1]D. Riley, Plasma Physics and Controlled Fusion **60**, 014033 (2018).
[2]S. H. Glenzer and R. Redmer, Rev. Mod. Phys. **81**, 1625 (2009).
[3]D. Kraus, T. Döppner, A. L. Kritcher, A. Yi, K. Boehm, B. Bachmann, L. Divol, L. B. Fletcher, S. H. Glenzer, O. L. Landen, N. Masters, A. M. Saunders, C. Weber, R. W. Falcone, and P. Neumayer, Journal of Physics: Conference Series **717**, 012067 (2016).
[4]D. Kraus, D. A. Chapman, A. L. Kritcher, R. A. Baggott, B. Bachmann, G. W. Collins, S. H. Glenzer, J. A. Hawreliak, D. H. Kalantar, O. L. Landen, T. Ma, S. Le Pape, J. Nilsen, D. C. Swift, P. Neumayer, R. W. Falcone, D. O. Gericke, and T. Döppner, Phys. Rev. E **94**, 011202 (2016).
[5]T. Döppner, A. L. Kritcher, P. Neumayer, D. Kraus, B. Bachmann, S. Burns, R. W. Falcone, S. H. Glenzer, J. Hawreliak, A. House, O. L. Landen, S. LePape, T. Ma, A. Pak, and D. Swift, Review of Scientific Instruments **85**, 11D617 (2014), https://doi.org/10.1063/1.4890253.
[6]B. Bachmann, A. L. Kritcher, L. R. Benedetti, R. W. Falcone, S. Glenn, J. Hawreliak, N. Izumi, D. Kraus, O. L. Landen, S. L. Pape, T. Ma, F. Pérez, D. Swift, and T. Döppner, Review of Scientific Instruments **85**, 11D614 (2014), https://doi.org/10.1063/1.4891303.
[7]B. Bachmann, T. Hilsabeck, J. Field, N. Masters, C. Reed, T. Pardini, J. R. Rygg, N. Alexander, L. R. Benedetti, T. Döppner, A. Forsman, N. Izumi, S. LePape, T. Ma, A. G. MacPhee, S. Nagel, P. Patel, B. Spears, and O. L. Landen, Review of Scientific Instruments **87**, 11E201 (2016), http://aip.scitation.org/doi/pdf/10.1063/1.4959161.
[8]B. Bachmann, H. Abu-Shawareb, N. Alexander, J. Ayers, C. G. Bailey, P. Bell, L. R. Benedetti, D. Bradley, G. Collins, L. Divol, T. Döppner, S. Felker, J. Field, A. Forsman, J. D. Galbraith, C. M. Hardy, T. Hilsabeck, N. Izumi, C. Jarrot, J. Kilkenny, S. Kramer, O. L. Landen, T. Ma, A. MacPhee, N. Masters, S. R. Nagel, A. Pak, P. Patel, L. A. Pickworth, J. E. Ralph, C. Reed, J. R. Rygg, and D. B. Thorn, in *Proc.SPIE*, Vol. 10390 (2017).
[9]B. Bachmann, R. Kozakov, G. Gött, K. Ekkert, J.-P. Bachmann, J.-L. Marques, H. Schöpp, D. Uhrlandt, and J. Schein, Journal of Physics D: Applied Physics **46**, 125203 (2013).
[10]S. A. Letts, D. W. Myers, and L. A. Witt, Journal of Vacuum Science and Technology **19**, 739 (1981), https://doi.org/10.1116/1.571142.
[11]V. A. Smalyuk, D. T. Casey, D. S. Clark, M. J. Edwards, S. W. Haan, A. Hamza, D. E. Hoover, W. W. Hsing, O. Hurricane, J. D. Kilkenny, J. Kroll, O. L. Landen, A. Moore, A. Nikroo, L. Peterson, K. Raman, B. A. Remington, H. F. Robey, S. V. Weber, and K. Widmann, Phys. Rev. Lett. **112**, 185003 (2014).
[12]K. S. Raman, V. A. Smalyuk, D. T. Casey, S. W. Haan, D. E. Hoover, O. A. Hurricane, J. J. Kroll, A. Nikroo, J. L. Peterson, B. A. Remington, H. F. Robey, D. S. Clark, B. A. Hammel, O. L. Landen, M. M. Marinak, D. H. Munro, K. J. Peterson, and J. Salmonson, Physics of Plasmas **21**, 072710 (2014), https://doi.org/10.1063/1.4890570.
[13]J. A. Oertel, R. Aragonez, T. Archuleta, C. Barnes, L. Casper, V. Fatherley, T. Heinrichs, R. King, D. Landers, F. Lopez, P. Sanchez, G. Sandoval, L. Schrank, P. Walsh, P. Bell, M. Brown, R. Costa, J. Holder, S. Montelongo, and N. Pederson, Review of Scientific Instruments **77**, 10E308 (2006), https://doi.org/10.1063/1.2227439.
[14]J. R. Kimbrough, P. M. Bell, D. K. Bradley, J. P. Holder, D. K. Kalantar, A. G. MacPhee, and S. Telford, Review of Scientific Instruments **81**, 10E530 (2010), https://doi.org/10.1063/1.3496990.
[15]L. R. Benedetti, J. P. Holder, M. Perkins, C. G. Brown, C. S. Anderson, F. V. Allen, R. B. Petre, D. Hargrove, S. M. Glenn, N. Simanovskaia, D. K. Bradley, and P. Bell, Review of Scientific Instruments **87**, 023511 (2016), https://doi.org/10.1063/1.4941754.